Formation of a Complex Active Center by Ba_2RuH_6 for Nondissociative Dinitrogen Activation and Ammonia Formation

Liu, Chuangwei; Wang, Qianru; Guo, Jianping; Vegge, Tejs; Chen, Ping; Hansen, Heine Anton

Published in:
ACS Catalysis

Link to article, DOI:
10.1021/acscatal.2c00180

Publication date:
2022

Document Version
Peer reviewed version

Ba_2RuH_6 Forming a Complex Active Center for Non-dissociative Dinitrogen Activation and Ammonia Formation

Chuangwei Liu,[1‡] Qianru Wang,[2,3‡] Jianping Guo,[2,3] Tejs Vegge,[1] Ping Chen,[2,3,4*] and Heine Anton Hansen[1*]*

[1]Department of Energy Conversion and Storage, Technical University of Denmark, 2800 Kgs. Lyngby, Denmark. [2]Dalian National Laboratory for Clean Energy, Dalian Institute of Chemical Physics, Chinese Academy of Sciences, Dalian, China. [3]University of Chinese Academy of Sciences, Beijing, China. [4]State Key Laboratory of Catalysis, Dalian, China. *Correspondence to: heih@dtu.dk ; pchen@dicp.ac.cn ; teve@dtu.dk. [‡]These authors contributed equally.

KEYWORDS ammonia synthesis; complex hydride; Ba_2RuH_6; non-dissociative N_2 activation; density function theory

ABSTRACT Mild-condition ammonia synthesis from N_2 and H_2 is a long-thought-after scientific goal and a practical need, especially for the intensively pursued “Green Ammonia” production using renewable H_2. Barium-containing materials have recently attracted significant attention as promising catalysts, catalyst supports, or mediators for effective ammonia synthesis under mild

conditions. Here, we report that the ternary barium-ruthenium complex hydride, Ba_2RuH_6, displays outstanding catalytic activity, which is nearly an order of magnitude higher than the active BaO promoted Ru metal (BaO-Ru/MgO) catalyst at temperatures below 573 K. Differing from the Ru metal catalyst, the kinetic parameters of Ba_2RuH_6 catalyst exhibit interesting temperature dependence. The catalytic center, function mechanism, and kinetic behaviors of Ba_2RuH_6 catalyst are investigated with a combined experimental and computational approach. We find that the N_2 reduction reaction (NRR) is preferentially carried out on a defected Ba_2RuH_6 (110) surface with Ba and H vacancies, in which a complex active center consisting of three Ba atoms and one Ru atom plus the coordinating hydridic hydrogens catalyze non-dissociative hydrogenolysis of N_2 through the dynamic and synergistic engagement of all the components of Ba_2RuH_6 in mediating electron and proton transfers. Specifically, the barium plays a unique and vital role in the whole process by directly donating electrons and bonding with reacting N_xH_y species. Based on the proposed reaction pathway, the catalytic and kinetic performances of the Ba_2RuH_6 catalyst are analyzed with the energetic span model, and the calculated turnover frequencies are comparable to the experimental results under the ammonia synthesis conditions applied in this study.

INTRODUCTION

At present, the global ammonia production exceeds 180 million metric tons, 90% of which is produced from high purity N_2 and H_2 gases under high temperatures and pressures (673-773 K, 10-30 MPa) via the Haber-Bosch process.[1-3] During the process, the inert dinitrogen triple bond is directly broken on the C_7 site of Fe catalyst or B_5 site of Ru catalyst via a dissociative

mechanism. This critical step is broadly viewed as the rate-determining step for ammonia synthesis.[4-5] However, the reliance on fossil fuels for H_2 production results in large energy consumption and CO_2 emissions.

Concerns of human-induced climate change are spurring an international scientific effort to decarbonize ammonia production. Over the last decade, momentum has been building to transform the conventional Haber-Bosch process towards the electrified Haber-Bosch (*e*HB) process that employs renewable, rather than fossil fuel sourced, hydrogen.[2, 6] One big challenge for achieving efficient *e*HB lies in the development of low-pressure and low-temperature ammonia synthesis catalysts, which contributes significantly to improving the compatibility of *e*HB with renewable electricity.

It is well known that supported Ru metal catalysts perform better than fused Fe catalysts for ammonia synthesis at lower pressures and temperatures.[7] Notably, the introduction of alkali or alkaline earth metal promoters can further enhance the performance of Ru metal.[8] In the 1990s, BaO was shown to be an effective promoter for Ru metal, but its specific role remains controversial.[9-10] Recently, Ba-containing compounds, such as oxyhydride $BaTiO_{0.5}H_{0.5}$, oxynitride-hydride $BaCeO_{3-x}N_yH_z$, and amide $Ba(NH_2)_2$, have also been employed as functional supports to boost N_2 dissociation on Ru metal.[11-13] Barium hydride BaH_2, on the other hand, can synergize with transition metals (such as Co, Ni, Mn) for effective mild-condition ammonia production via either catalytic or chemical looping processes, where BaH_2 directly participates in the dinitrogen activation and ammonia formation.[14-16] Very recently, a barium-chromium nitride hydride [BaCrHN] catalyst was reported to exhibit activities higher than the benchmark Cs_2O-Ru/MgO catalyst at low temperatures.[17] Therefore, the role of Ba could be multi-functional as it is an indispensable component of promoter, support, (co)catalyst, or mediator for facilitating

ammonia production under mild conditions. It is, however, a highly challenging research topic in unveiling the molecular-level mechanism of Ba in advancing ammonia formation, as manifested by minimal investigations.[10]

A recent study demonstrated that Ba, Ru, and H could compound into a complex hydride Ba_2RuH_6, which catalyzes ammonia synthesis extraordinarily well under mild conditions.[18] Nonetheless, the mechanistic details for dinitrogen reduction and ammonia formation over Ba_2RuH_6 catalyst are underexplored. In this unique catalytic system, both Ba and Ru elements are catalytic components, and Ru is no longer in a metallic state. Typically, the transition metal is considered as the center for N_2 activation. However, this view is challenged by several recent studies, in which the activation of N_2 has been demonstrated to take place on the alkali or alkaline metal center.[15, 19] Specifically, for the soluble Ca system reported very recently, the role of Ca *d* orbitals for N_2 binding has been discussed.[19] In such a scenario, it would be very intriguing to probe into the mechanistic details of N_2 reduction reaction (NRR) that occurs on the surface of Ba_2RuH_6 catalyst. Herein, with a combination of experimental and theoretical work, we find that the key to achieving efficient NH_3 synthesis lies in the unique configuration and reaction mechanism of the Ba_2RuH_6 catalyst. Ba_2RuH_6 itself forms a kind of multi-functional and redox-active catalytic center for synergized and non-dissociative N_2 reduction, where Ba provides the site for N_2 activation and H_2 dissociation, Ru and Ba cooperate in the subsequent N_2 reduction and hydrogenation, and hydridic hydrogens synergize with surrounding Ba and Ru in mediating electron transfers. These fundamental understandings obtained from this work have the potential to devise catalyst development towards mild-condition green ammonia synthesis.

RESULTS AND DISCUSSION

1. Catalytic and kinetic performance

Figure 1a compares the ammonia synthesis rates of complex hydride Ba_2RuH_6 catalyst with some Ru metal reference catalysts, including Ru/MgO, Cs_2O promoted Ru/MgO (Cs_2O-Ru/MgO), and BaO-promoted Ru/MgO (BaO-Ru/MgO) catalysts. At 573 K and 1 bar, the MgO-supported Ba_2RuH_6 catalyst (Ba_2RuH_6/MgO), with an effective exposure of the complex hydride sites, produces NH_3 at a rate that is ca. 25, 6.3, and 9.5 times higher than the active Ru/MgO, Cs_2O-Ru/MgO, and BaO-Ru/MgO catalysts, respectively. This advantage becomes more apparent at lower temperatures (Figure 1a). We also note that the NH_3 yield of Ba_2RuH_6/MgO is reaching the thermodynamic limit at 598 K under a space velocity of 7500 ml g_{cat}^{-1} h^{-1} (Figure S1).

Of particular interest is the temperature-dependent kinetic parameters of the Ba_2RuH_6 complex hydride catalyst. As shown in Figure 1b, the Arrhenius plot of Ba_2RuH_6 catalyst has an inflection point at around 523 K. The catalyst has a smaller apparent activation energy (63.9 kJ mol^{-1}) at temperatures higher than 523 K and a significantly larger value of 90.3 kJ mol^{-1} at temperatures below 523 K. In contrast, there is no observable change in activation energy for conventional Ru metal catalyst (Ru/MgO) in a wide temperature range (498-648 K). Moreover, the reaction orders of H_2 and NH_3 for Ba_2RuH_6 catalyst also vary with temperature (Figures 1c-d). The Ba_2RuH_6 catalyst exhibits a positive reaction order with respect to H_2 at 573 K ($\gamma(H_2, 573\ K) = +1.0$), in clear contrast to the Ru/MgO catalyst that has severe hydrogen poisoning effect and thereby shows a negative H_2 that close to -1 (Figure S2b).[20] At temperatures below 523 K, however, the Ba_2RuH_6 catalyst is also subject to moderate hydrogen poisoning, as the H_2 reaction orders measured at 473 K is $\gamma(H_2, 473\ K) = -0.49$. With the increase of temperature, the NH_3 inhibiting effect strengthens, as the NH_3 reaction order decreases from $\alpha(NH_3, 473\ K) = -0.39$ to

$\alpha(NH_3, 573\ K) = -0.63$. In the whole testing temperature range, the reaction order of N_2, $\beta(N_2)$, is close to 1 (Figure S3). It can be concluded that the competitive adsorption of H_2 and NH_3 over the Ba_2RuH_6 catalyst is temperature-dependent, and the preference of H_2 over NH_3 is enhanced as the temperature grows.

Given the above, it can be clearly seen that the chemical composition, high catalytic performance, and temperature-dependent kinetic behaviors of Ba_2RuH_6 catalyst are significantly different from conventional Ru metal catalyst (Figure 1 and Figure S2), underlying the unique active center and reaction mechanism of this complex hydride catalyst.

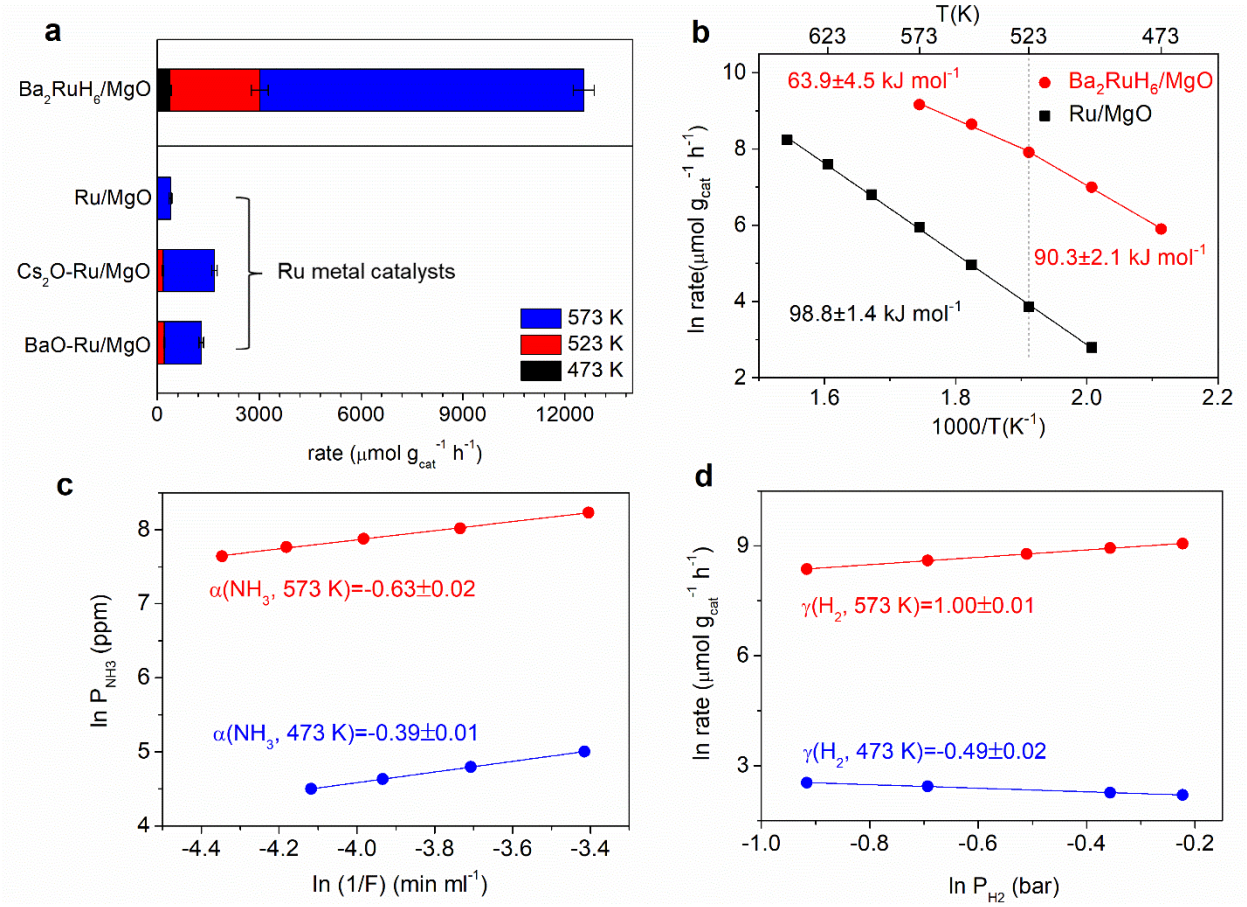

Figure 1. (a) Comparison of NH_3 synthesis rates of Ba_2RuH_6 catalyst and Ru metal-based reference catalysts. Reaction conditions: catalyst loading, 30mg; N_2:H_2=1:3; flow rate, 30 ml min^{-1}; pressure, 1 bar. (b) Arrhenius plots of Ba_2RuH_6/MgO and Ru/MgO catalyst in the temperature range of 473-648 K. (c) to (d) dependence of ammonia synthesis rates on the partial pressures of NH_3 and H_2, respectively, under a total pressure of 1 bar and at 573 K (red circles) and 473 K (blue circles) over Ba_2RuH_6/MgO catalyst.

2. Exploration of the potential active surface

To ascertain the active phase of the hydride catalyst, X-ray diffraction (XRD) characterization of the tested Ba_2RuH_6/MgO has been performed. As shown in Figure S4a, Ba_2RuH_6/MgO catalyst after ammonia synthesis test has diffraction peaks attributable to the Ba_2RuH_6 phase, which demonstrates that Ba_2RuH_6 dominates the active phase. In addition, the Fourier transform infrared (FT-IR) measurement shows a broad peak assignable to Ru-H stretching vibration (Figure S4b), indicating that the Ba_2RuH_6 surface has intriguing flexibility in accommodating hydridic hydrogens. Nevertheless, the atomic-level identification of the active center over the Ba_2RuH_6 surface by experiment is difficult considering the complex nature of this multi-component surface.

To better understand the mechanistic details behind the unique performance of Ba_2RuH_6 catalyst, DFT calculations are thereby employed. The conventional unit cell of Ba_2RuH_6 is shown in Figure 2a, where ionic Ru binds with six hydridic hydrogens forming octahedral $[RuH_6]^{4-}$ anions that are stabilized by the surrounding Ba^{2+} cations. In other words, the Ba^{2+} cations form a K_2PtCl_6-type framework to isolate the electron-rich $[RuH_6]^{4-}$ anions spatially.[21] Based on the XRD pattern of Ba_2RuH_6 (Figure 2b), three low-Miller-index surfaces including (111), (100),

and (110) are cleaved from the primitive cell to explore the active surface of Ba_2RuH_6 catalyst, as shown in Figures 2c, 2d, and S5. By comparing the optimized structures, layered energies, and work functions of these three surfaces (Figures S5-7), the following conclusions can be obtained: 1) (100) and (111) are equivalent surfaces; 2) (110) has the lowest work function; and 3) two-layer cleaved slabs can represent the corresponding surface. Besides, some possible defected surfaces are built by creating H and/or Ba vacancies on the pristine (100) and (110) surfaces, which are denoted as $V(Ba_xH_y)$. For example, V(BaH) represents creating one Ba vacancy and one H vacancy. The thermodynamic stability of these defected surfaces is evaluated by the formation free energy under experimental conditions (573 K and 1 bar), and the calculated results are presented in Figures 2e, 2f, S8, and S9. It can be learned that the pristine (100) is the most stable surface, and any vacancies formed on this surface cost considerable energy (Figure 2e). While for the (110) surface, several cases, including V(Ba), $V(Ba_2)$, $V(Ba_3)$, V(BaH), $V(Ba_2H)$, and $V(Ba_3H)$, are thermodynamic neutral or favorable during vacancy formation (Figure 2f). Therefore, the relatively stable surfaces, including pristine (100), pristine (110), and six defected (110) (i.e., V(Ba), $V(Ba_2)$, $V(Ba_3)$, V(BaH), $V(Ba_2H)$, $V(Ba_3H)$) surfaces are further investigated for the activation of N_2 and H_2 molecules.

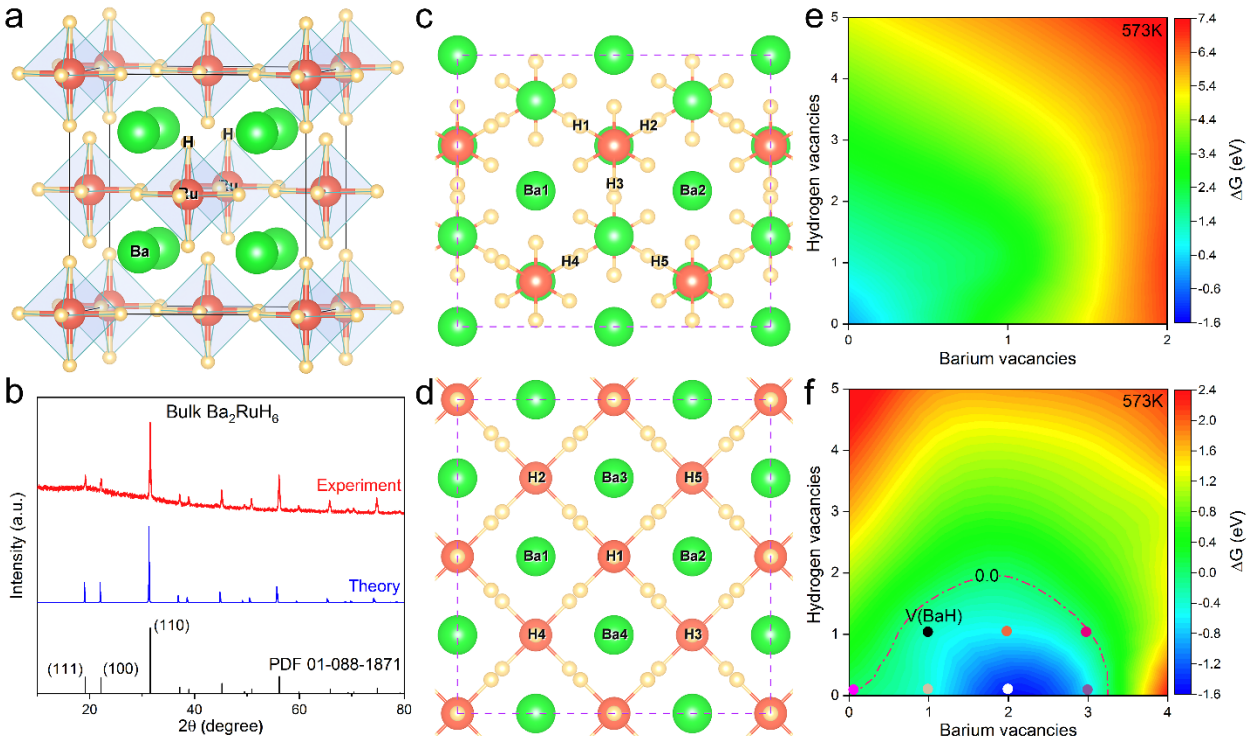

Figure 2. (a) Conventional cell of Ba_2RuH_6. (b) Experimental and theoretical-derived X-ray diffraction patterns of Ba_2RuH_6. Top views of the optimized pristine (100)/(111) surface (c) and pristine (110) surface (d). Relative formation free energy of Ba and/or H vacancies on pristine (100)/(111) surface (e) and pristine (110) surface (f) under 573 K and 1 bar. Green, red, and yellow spheres represent Ba, Ru, and H, respectively. The specific positions of H and/or Ba vacancies created on (100)/(111) or (110) surface are marked by numbers in (c) or (d).

The optimized configurations of N_2 adsorption on the selected pristine and defected surfaces are shown in Figures S10 and S11, respectively. It can be seen that the N_2 molecule can adsorb on the pristine and defected (110) surfaces (side-on mode for pristine, V(Ba), V(BaH), V(Ba_2), and V(Ba_2H), and end-on mode for V(Ba_3) and V(Ba_3H)), but not on the pristine (100) surface. For the (110) surface, N_2 adsorption is most substantial on the pristine surface and becomes weakened with the increase of Ba vacancies (Figure 3a and Figure S12). It is important to note

that, for these pristine and defected (110) surfaces, the surface Ba sites rather than Ru are responsible for binding N_2. Several cases, such as N_2 chemisorption on pristine, V(Ba), and V(BaH) (110) surfaces, along with the corresponding charge density differences, are presented in Figure 3b, where surface Ba sites transfer most electrons to the adsorbed N_2, showing the indispensable role of Ba in N_2 chemisorption. In addition, investigations of H_2 chemisorption suggest that these seven pristine and defected (110) surfaces are incapable of binding the H_2 molecule prior to N_2 binding (Figure S13), which is distinct from the Ru metal surface that facilely dissociates H_2 molecule into surface hydrogens. [22] The dissociative adsorption of H_2 is, however, in some cases favorable on the surface H vacancies as shown in Figure 2f.

Beyond that, the chemisorption of N_2 over the pristine and defected (110) surfaces has a unique fingerprint: the number of Ba vacancies has a linear impact on the extent of N_2 activation. As shown in Figure 3c, for the (110) surface, the degree of N_2 activation gradually lessens with the increasing number of Ba vacancies, as reflected by the decreased N-N bond length and the increased Bader charge of adsorbed N_2 (denoted as N_2*). A similar variation can be observed on the (110) surfaces with an extra H vacancy. In contrast, the extent of N_2 activation becomes stronger compared to that of the surface with only Ba vacancies. The charge transfer from Ba atoms to N_2, explains the perhaps surprising result that H_2 binds less strongly with a decrease in the concentration of Ba vacancies. These calculation results indicate the strong connection between N_2 activation and the surface composition of the Ba_2RuH_6 catalyst, which further underlines the importance of Ba in N_2 activation.

Two mechanistic proposals for NRR are discussed in the literature: I. the dissociative mechanism, where the N-N triple bond dissociates completely before any hydrogenation takes place; II. the associative mechanism, where N_2 undergoes hydrogenation to N_2H_x via a distal or

alternating pathway prior to splitting the N-N bond.[3] Catalytic NRR on the surface of conventional Ru or Fe metal surface is usually believed to follow the dissociative mechanism. We hereinafter investigate the NRR pathways on the seven potential surfaces of Ba_2RuH_6 catalyst, that is pristine, V(Ba), V(Ba_2), V(Ba_3), V(BaH), V(Ba_2H), and V(Ba_3H) (110) surfaces, under experimental conditions (573 K and 1 bar). As shown in Figure S14, the calculated barriers for N_2* direct dissociation are higher than 1.96 eV on these potential model surfaces. By contrast, the associative hydrogenation of N_2* to NNH* has moderate barriers. For example, the calculated barrier for hydrogenation of N_2* to NNH* on V(BaH) surface is as low as 0.73 eV (Figure S15), indicating the associative pathway is kinetically more favorable. Therefore, the associative mechanism for ammonia synthesis, including the distal and alternating pathways, is further investigated on the above seven potential model surfaces with N_2 and H_2 as the feeding gas, as shown in Figure S16. The thermodynamic energetic spans of the distal and alternating reaction pathways over the seven potential surfaces are summarized in Figure 3d, among which the distal reaction pathway occurred on the V(BaH) surface was found to display the minimum thermodynamic energetic span (0.83 eV) that is substantially lower by > 0.8 eV than the others. Although N_2 is adsorbed most strongly on the pristine (110) surface, its thermodynamic energetic span is high because NH_2* binds strongly to such surface.

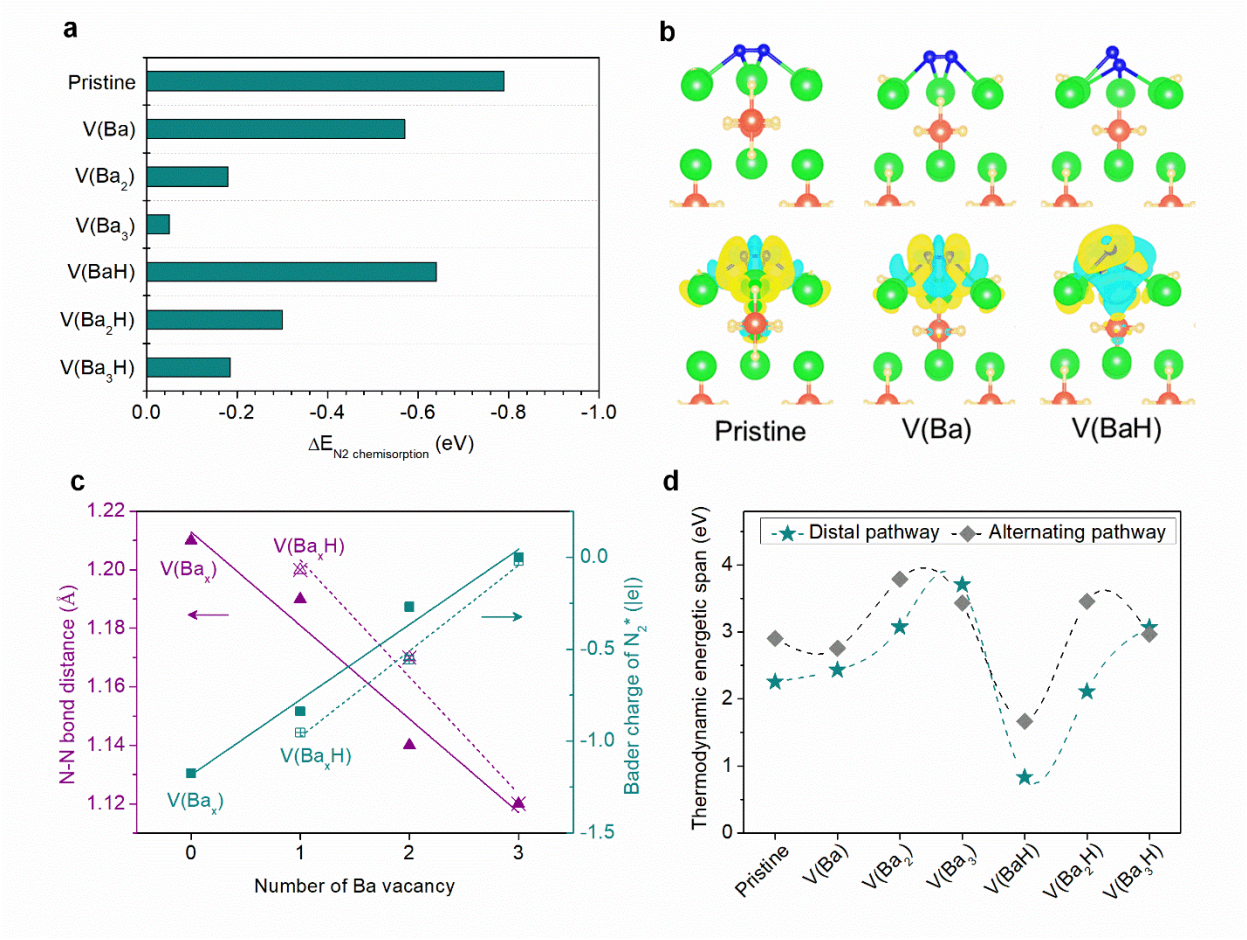

Figure 3. (a) Energies of N_2 chemisorption on pristine, V(Ba), V(BaH), V(Ba_2), V(Ba_2H), V(Ba_3), and V(Ba_3H) (110) surfaces. (b) Optimized configurations and the corresponding charge density differences of N_2 chemisorption on pristine, V(Ba), and V(BaH) (110) surfaces. The isosurface value is set to be 0.003 e $Å^{-3}$, and the charge accumulation and loss are shown in yellow and cyan, respectively. (c) Bond distances and Bader charges of adsorbed N_2 on Ba-defected-(110) surface with or without an extra H vacancy as a function of Ba vacancy number. (d) Thermodynamic energetic spans of the catalytic cycle on the pristine, V(Ba), V(BaH), V(Ba_2), V(Ba_2H), V(Ba_3), and V(Ba_3H) (110) surfaces via a distal pathway or an alternating pathway. The thermodynamic energetic spans were calculated at 573 K and 1 bar (H_2/N_2 ratio is

fixed at 3:1 and the ammonia concentration is fixed at 0.39%, which is consistent with the experimental conditions).

3. Reaction mechanism and electronic structure

The full free energy diagram of the distal reaction pathway on the V(BaH) surface, as well as the optimized structure of each N_xH_y+nH* intermediate state along the path (where H* represents the dissociated H from H_2), have been mapped out using DFT calculations. As shown in Figure 4, a Ba_3RuH_x complex hydride cluster consisting of three Ba atoms and one Ru atom plus the coordinating hydridic hydrogens is identified as the active center for mediating N_2 activation and NH_3 formation. Meanwhile, the Bader charges of each N_xH_y+nH* intermediate, as well as the surrounding Ba, Ru, and lattice hydride, have been calculated, as depicted in Figure 5a. The Ba-N, Ru-N, and N-N distance along the reaction pathway have also been tracked (Figure 5b).

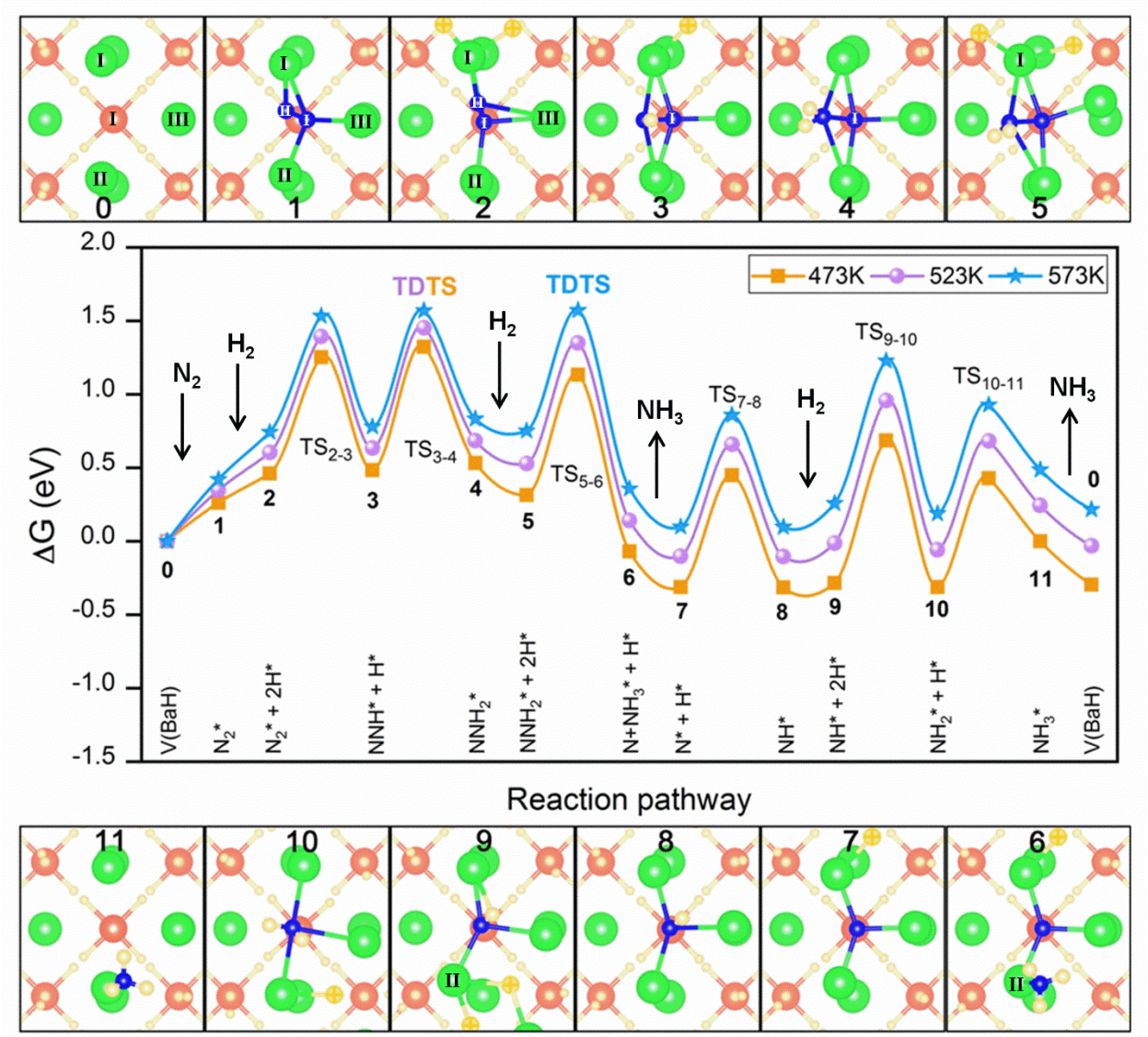

Figure 4. Free energy diagrams of the distal reaction pathway on V(BaH) surface of $Ba_2RuH_6(110)$. Color code: Ru-orange, H-yellow, Ba-green, and N-blue. Note that the dark yellow atoms with a cross mark represent H from dissociated H_2. The free energy pathways were calculated at 573 K and 1 bar (H_2/N_2 ratio is fixed at 3, and the ammonia concentrations at 573 K, 523 K, and 423 K are 0.39%, 0.11%, and 0.015%, respectively, which are consistent with the experimental conditions). At temperatures at or below 523 K, the TDTS and TDI are $TS_{3\text{-}4}$ and **8**,

respectively. At temperatures above 523 K, the TDTS and TDI are $TS_{5\text{-}6}$ and **8**, respectively. The configurations of the transition states are presented in Figure S17.

Initially, N_2 prefers to chemisorb on Ba sites instead of a Ru site (**0**-**1**), in which the upper N (denoted as N^{II}) and lower N (denoted as N^{I}) atoms are coordinated by one and three Ba atoms, respectively. The Ba-N distance is between 2.74 and 2.89 Å with an average value of 2.85 Å, while the Ru-N distance is longer than 3.61 Å. After N_2 chemisorption, the bond order of N_2 is reduced to 2.5, with its bond length of 1.21 Å. Our Bader charge analyses reveal that N_2 gains 0.91 |e| from its surrounding Ba, Ru, and lattice hydride species, in which Ba atoms donate the most electrons to N_2. To elucidate the bonding nature of the species involved in step **0**-**1**, the projected densities of states (PDOS) of N_2 adsorption on the V(BaH) surface are calculated. As depicted in Figure 5c, the energy levels of the Ba d orbitals and N_2 π^* orbitals are well-matched near the Fermi level. In contrast, there is no apparent interaction between Ru d orbitals and N_2 π^* orbitals. Therefore, it can be concluded that the d orbitals of Ba play a leading role in the chemisorption of N_2, showing similar characteristics with the N_2 activation on the recently reported molecular Ca complex.[19]

Before hydrogenating the adsorbed N_2, H_2 prefers to undergo dissociative adsorption on the Ba^{I} site (step **1**-**2**) of the active surface. Ru^{I} starts to interact with the adsorbed N_2 as the Ru^{I}-N^{I} distance drops from 3.61 to 2.15 Å. Note that the activation of H_2 becomes facile after N_2 chemisorption and the barrier for dissociative H_2 adsorption on V(BaH) surface is as low as 0.09 eV (Figure S18), which can be neglected comparably. Our Bader charge analyses show that N_2* and the two dissociated H* species receive 0.14 |e| and 0.99 |e| from the surrounding catalytic environment, respectively, i.e., a total of 1.13 |e| gain for the N_2*+2H* state. Nevertheless, the N-N bond length is shortened slightly, mainly owing to the steric hindrance from the involved H*

species. Similarly, the bonding nature of the species involved in step **1**-**2** was investigated through the PDOS analyses. As presented in Figure S19, both Ba d orbitals and Ru d orbitals overlap with N_2 π* orbitals, making it evident that both Ba and Ru are involved in the N_2 activation when the first H_2 dissociates onto the active surface.

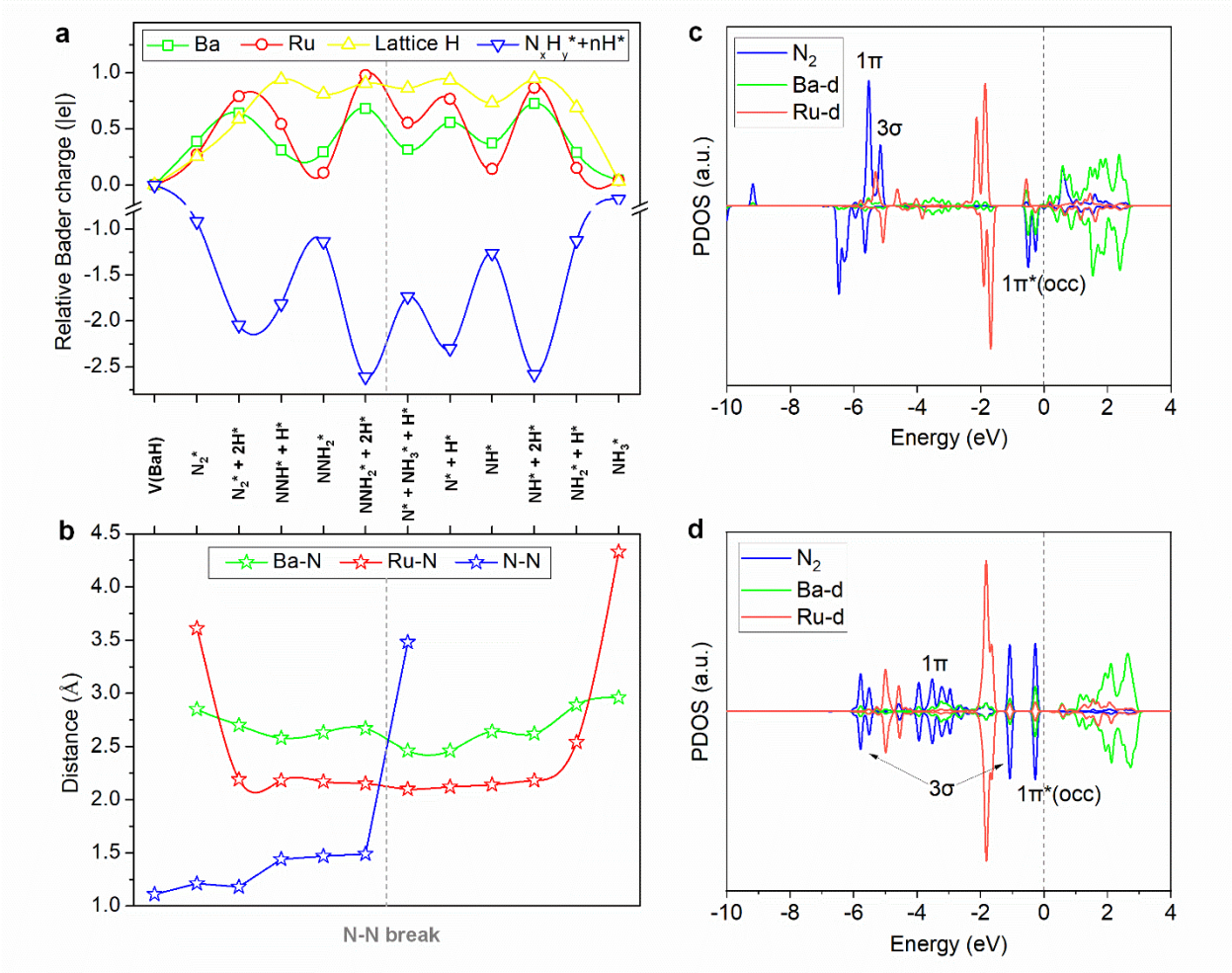

Figure 5. (a) Bader charge analyses of the N_xH_y absorbate and its surrounding catalytic environment, including the Ba, Ru, and lattice H components, at every step of the catalytic cycle. The changes in the Bader charge (i.e., relative Bader charge) are relative to the initial state. (b) Distances of Ba-N, Ru-N, and N-N along the reaction pathway. The Ba-N distance represents an average bond distance of Ba^{I}-N^{II}, Ba^{I}-N^{I}, Ba^{II}-N^{I}, and Ba^{III}-N^{I}. The Ru-N distance represents the

distance between Ru^{I} and N^{I}. (c) and (d) are the projected density of states (PDOS) of N_2* and NNH* intermediate states, respectively.

In the following steps, hydrogenation occurs preferentially via a distal pathway. Specifically, the N atom away from the catalyst surface (i.e., N^{II}) is first attacked by the dissociated H atoms, leading to the release of one NH_3 molecule (steps **2**-**3**-**4**-**5**-**6**). And then, the remaining N atom continues the hydrogenation process to produce the second NH_3 molecule (steps **7**-**8**-**9**-**10**-**11**). As shown in Figures 4, 5a, and 5b, the first (step **2**-**3**) and second (step **3**-**4**) hydrogenation steps happen from the two dissociated hydrogens on Ba^{I} site with kinetic barriers of 0.79 and 0.79 eV, respectively. After these two hydrogenation steps, the N-N bond length is then elongated to 1.47 Å, and the bond distances of Ba-N and Ru-N remain nearly constant. Bader charges of NNH_2* turn to -1.14 |e|. Then a second H_2 dissociates into two hydrogens on the Ba^{I} site again (step **4**-**5**), and one H* attacks the NNH_2* with a kinetic barrier of 0.82 eV (step **5**-**6**), leading to the cleavage of the N-N bond and the formation of the first ammonia. The formed NH_3* leaves Ru and hangs loosely on the neighboring Ba (i.e., Ba^{II}) and then desorbs from the surface (step **6**-**7**). Next, the remaining N* species consumes three H* (one from the second dissociated H_2 and two from the third dissociated H_2), creating NH* (step **7**-**8**), NH_2* (step **9**-**10**), and the second NH_3* (step **10**-**11**) species gradually. Note that the third H_2 prefers to dissociate on the Ba^{II} site. The kinetic barriers for these three successive hydrogenation steps are 0.76, 0.97, and 0.74 eV, respectively. After the desorption of the second NH_3 from the Ba^{II} site, the surface restores the initial state (step **11**-**0**). In all hydrogenation steps along the pathway, the Ba-N bond distances vary within a narrow range of 2.46-2.89 Å, and Ru-N bond distances within 2.12-2.54 Å before forming the second ammonia. What's more, our study shows that Ru synergizes with Ba to mediate hydrogen transfers, as supported by the PDOS analyses of the representing states (i.e.,

NNH* and NH_2*) of the hydrogenation process (Figures 5d and Figure S20). It can be seen the NN π* orbitals in NNH* state (Figure 5d) or N p orbitals in NH_2* state (Figure S20) interact with both Ru d orbitals and Ba d orbitals, indicating the collaborative involvement of Ba and Ru in mediating the hydrogenation of activated N_2 to NH_3.

It is important to point out that the Ba_3RuH_x active center serves as an electron reservoir to regulate the charge variation of the whole catalytic process, which donates electrons at the adsorption steps and accepts electrons at the hydrogenation steps via the interplay of all its components, as depicted in Figure 5a. In addition, such complex active center is multi-functional: Ba for the initial N_2 activation step and the H_2 dissociation steps, and the cooperation of Ba and Ru for the subsequent hydrogenation and ammonia formation steps. Therefore, it can be concluded that the barium ruthenium complex hydride itself forms a multi-functional and redox-active center, which enables an energetically favorable reaction pathway for effective ammonia production through the dynamic and engagement of all its active components in catalysis.

4. Kinetic analysis

To better understand the catalytic and kinetic performance of Ba_2RuH_6 catalyst, the variations of the reaction energetics as a function of temperature are explored and then analyzed by applying the energetic span model, in which the TOF-determining transition state (TDTS) and the TOF-determining intermediate (TDI) that maximize the energetic span determine the rates and kinetics of the catalytic cycle.[23] Figure 4 and Figure S21 show the development of the free energy path over the active surface of Ba_2RuH_6 catalyst from 473 to 573 K, the applied temperature range in the experimental studies shown in Figure 1. By analyzing the TDTS and TDI of the free energy

path at each temperature, we find that the change in reaction temperature shifts the TDTS of the catalytic cycle, with an inflection temperature around 523 K. The TDTS moves from transition state $TS_{3\text{-}4}$ to $TS_{5\text{-}6}$ as the temperature goes above the inflection point at 523 K. Such a feature is correlated with the experimental observations that the apparent activation energies and the H_2 and NH_3 reaction orders of Ba_2RuH_6 catalyst change at 523 K (Figures 1b, 1c and 1d). This correlation implies that the unique temperature-dependent kinetic behaviors observed for Ba_2RuH_6 catalyst are attributable to the shift of the rate-determining states (i.e., the TDTS) along the reaction pathway. Around 523 K, the increase in temperature shifts the TDTS from $TS_{3\text{-}4}$ to $TS_{5\text{-}6}$ as the adsorption of H_2 separating the two transition states becomes increasingly difficult at increasing temperatures. The resulting change in the TDTS directly affects the microkinetic kinetic behaviors of the catalyst, such as the apparent activation energies and the reaction order of H_2.

At a given temperature, the turnover frequency (TOF) of Ba_2RuH_6 catalyst can be further estimated from the energetic span of the free energy path.[23] The theoretical-derived TOFs are compared to the experimental-derived TOFs within the temperature range applied in this study, as presented in Figure 6. It can be seen that there is an increase in TOF as the temperature rises, and the theoretical-derived TOFs are comparable to the experimental-derived TOFs within the allowed error range. Such an agreement further verifies the rationality of the proposed reaction mechanism.

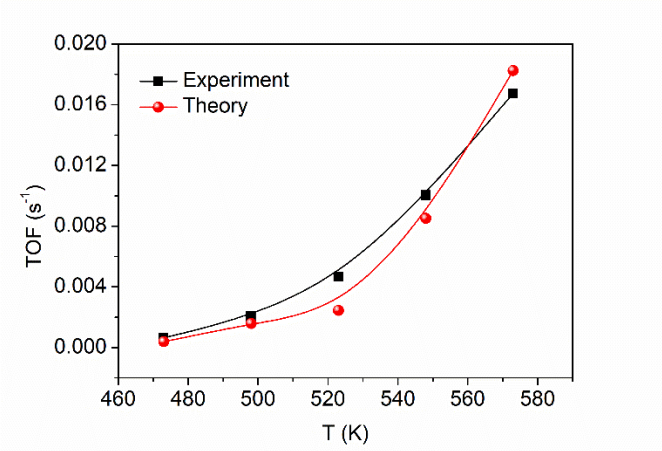

Figure 6. Comparison of the theoretical- and experimental- derived TOF in the temperature range of 473-573 K. The experimental TOF was estimated based on the surface ruthenium content derived from the average particle size observed by transmission electron microscopy (Figure S22) and assuming spherical particle morphology.

CONCLUSIONS

This work presents a mechanistic investigation of the Ba_2RuH_6 catalyst for mild-condition ammonia synthesis. Results from the synchronized experimental and theoretical studies show that, in clear contrast to the Ru metal-based catalysts, the Ba_2RuH_6 complex hydride prefers a synergistic and non-dissociative reaction pathway with a narrow energetic span and perfectly balanced kinetic barriers for the multiple hydrogenation steps, which leads to catalytic ammonia synthesis from N_2 and H_2 with excellent performance under mild conditions. Such mechanism shares some common features with that of Li_4RuH_6 catalyst system, but the Ba component of the Ba_2RuH_6 catalyst plays certain different roles from the Li component of Li_4RuH_6 catalyst in that the latter mainly co-stabilizes N_xH_y species through electrostatic interactions,[18] whereas the former participates in the whole process, including the initial N_2 activation, the H_2 dissociation,

the subsequent hydrogenation, and ammonia formation steps, through direct bonding with the N_xH_y intermediates. Additionally, the simulated kinetic performances of the Ba_2RuH_6 catalyst agree well with the experimental results, strengthening the rationality of the proposed reaction mechanism. These scientific findings enrich our fundamental understandings of the chemistry of nitrogen reduction reaction and may provide new insights on the rational design and development of catalyst materials towards greener ammonia synthesis.

ASSOCIATED CONTENT

Supporting Information. The Supporting Information is available free of charge at DOI: xxx.

AUTHOR INFORMATION

Corresponding Authors

Heine Anton Hansen—Department of Energy Conversion and Storage, Technical University of Denmark, 2800 Kgs. Lyngby, Denmark. orcid.org/0000-0001-7551-9470; Email: heih@dtu.dk

Ping Chen—Dalian National Laboratory for Clean Energy, Dalian Institute of Chemical Physics, Chinese Academy of Sciences; State Key Laboratory of Catalysis, Dalian, 116023, China. orcid.org/0000-0002-0625-0639; Email: pchen@dicp.au.cn

Tejs Vegge—Department of Energy Conversion and Storage, Technical University of Denmark, 2800 Kgs. Lyngby, Denmark. orcid.org/0000-0002-1484-0284; Email: teve@dtu.dk

Authors

Chuangwei Liu—Department of Energy Conversion and Storage, Technical University of Denmark, 2800 Kgs. Lyngby, Denmark. orcid.org/0000-0002-8256-6053

Qianru Wang—Dalian National Laboratory for Clean Energy, Dalian Institute of Chemical Physics, Chinese Academy of Sciences, Dalian, 116023, China; University of Chinese Academy of Sciences, Beijing, 100049, China. orcid.org/0000-0001-8680-4162

Jianping Guo—Dalian National Laboratory for Clean Energy, Dalian Institute of Chemical Physics, Chinese Academy of Sciences; Collaborative Innovation Center of Chemistry for Energy Materials, Dalian, 116023, China. orcid.org/0000-0002-0229-8555

Author Contributions

The manuscript was written through contributions of all authors. All authors have given approval to the final version of the manuscript. ‡These authors contributed equally.

Notes

The authors declare no competing financial interest.

ACKNOWLEDGMENT

C. L., H. H., and T. V. thank the Villum Foundation for financial support through the research center V-Sustain (#9455). Q. W., J. G., and P. C. thank the financial support from National Key R&D Program of China (No. 2021YFB4000401), National Natural Science Foundation of China (Grant Nos. 21922205, 21988101, and 21872137), Youth Innovation Promotion Association CAS (No. 2018213), Liaoning Revitalization Talents Program (XLYC2007173, XLYC2002076), and K. C. Wong Education Foundation (GJTD-2018-06).

REFERENCES

1. MacFarlane, D. R.; Cherepanov, P. V.; Choi, J.; Suryanto, B. H. R.; Hodgetts, R. Y.; Bakker, J. M.; Ferrero Vallana, F. M.; Simonov, A. N. A Roadmap to the Ammonia Economy. *Joule* **2020,** *4* (6), 1186-1205.

2. Ye, L.; Nayak-Luke, R.; Bañares-Alcántara, R.; Tsang, E. Reaction: "Green" Ammonia Production. *Chem* **2017,** *3* (5), 712-714.

3. Wang, Q.; Guo, J.; Chen, P. Recent progress towards mild-condition ammonia synthesis. *J. Energy Chem.* **2019,** *36*, 25-36.

4. Ertl, G. Reactions at Surfaces: From Atoms to Complexity (Nobel Lecture). *Angew. Chem. Int. Ed.* **2008,** *47* (19), 3524-3535.

5. Honkala, K.; Hellman, A.; Remediakis, I. N.; Logadottir, A.; Carlsson, A.; Dahl, S.; Christensen, C. H.; Nørskov, J. K. Ammonia Synthesis from First-Principles Calculations. *Science* **2005,** *307* (5709), 555-558.

6. Smith, C.; Hill, A. K.; Torrente-Murciano, L. Current and future role of Haber–Bosch ammonia in a carbon-free energy landscape. *Energy & Environ. Sci.* **2020,** *13* (2), 331-344.

7. Brown, D. E.; Edmonds, T.; Joyner, R. W.; McCarroll, J. J.; Tennison, S. R. The Genesis and Development of the Commercial BP Doubly Promoted Catalyst for Ammonia Synthesis. *Catal. Lett.* **2014,** *144* (4), 545-552.

8. Aika, K.-i. Role of alkali promoter in ammonia synthesis over ruthenium catalysts—Effect on reaction mechanism. *Catal. Today* **2017,** *286*, 14-20.

9. Bielawa, H.; Hinrichsen, O.; Birkner, A.; Muhler, M. The Ammonia-Synthesis Catalyst of the Next Generation: Barium-Promoted Oxide-Supported Ruthenium. *Angew. Chem. Int. Ed.* **2001,** *40* (6), 1061-1063.

10. Hansen, T. W.; Wagner, J. B.; Hansen, P. L.; Dahl, S.; Topsøe, H.; Jacobsen, C. J. Atomic-resolution in situ transmission electron microscopy of a promoter of a heterogeneous catalyst. *Science* **2001,** *294* (5546), 1508-1510.

11. Tang, Y.; Kobayashi, Y.; Masuda, N.; Uchida, Y.; Okamoto, H.; Kageyama, T.; Hosokawa, S.; Loyer, F.; Mitsuhara, K.; Yamanaka, K.; Tamenori, Y.; Tassel, C.; Yamamoto, T.; Tanaka, T.; Kageyama, H. Metal-Dependent Support Effects of Oxyhydride-Supported Ru, Fe, Co Catalysts for Ammonia Synthesis. *Adv. Energy Mater.* **2018,** *8* (36), 1801772.

12. Kitano, M.; Inoue, Y.; Sasase, M.; Kishida, K.; Kobayashi, Y.; Nishiyama, K.; Tada, T.; Kawamura, S.; Yokoyama, T.; Hara, M.; Hosono, H. Self-organized Ruthenium–Barium Core–Shell Nanoparticles on a Mesoporous Calcium Amide Matrix for Efficient Low-Temperature Ammonia Synthesis. *Angew. Chem. Int. Ed.* **2018,** *57* (10), 2648-2652.

13. Kitano, M.; Kujirai, J.; Ogasawara, K.; Matsuishi, S.; Tada, T.; Abe, H.; Niwa, Y.; Hosono, H. Low-Temperature Synthesis of Perovskite Oxynitride-Hydrides as Ammonia Synthesis Catalysts. *J. Am. Chem. Soc.* **2019,** *141* (51), 20344-20353.

14. Gao, W.; Wang, P.; Guo, J.; Chang, F.; He, T.; Wang, Q.; Wu, G.; Chen, P. Barium Hydride-Mediated Nitrogen Transfer and Hydrogenation for Ammonia Synthesis: A Case Study of Cobalt. *ACS Catal.* **2017,** *7* (5), 3654-3661.

15. Gao, W.; Guo, J.; Wang, P.; Wang, Q.; Chang, F.; Pei, Q.; Zhang, W.; Liu, L.; Chen, P. Production of ammonia via a chemical looping process based on metal imides as nitrogen carriers. *Nat. Energy* **2018,** *3* (12), 1067-1075.

16. Feng, S.; Gao, W.; Wang, Q.; Guan, Y.; Yan, H.; Wu, H.; Cao, H.; Guo, J.; Chen, P. A multi-functional composite nitrogen carrier for ammonia production via a chemical looping route. *J. Mater. Chem. A* **2021,** *9* (2), 1039-1047.

17. Guan, Y.; Zhang, W.; Wang, Q.; Weidenthaler, C.; Wu, A.; Gao, W.; Pei, Q.; Yan, H.; Cui, J.; Wu, H.; Feng, S.; Wang, R.; Cao, H.; Ju, X.; Liu, L.; He, T.; Guo, J.; Chen, P. Barium chromium nitride-hydride for ammonia synthesis. *Chem Catal.* **2021,** *1* (5), 1042-1054.

18. Wang, Q.; Pan, J.; Guo, J.; Hansen, H. A.; Xie, H.; Jiang, L.; Hua, L.; Li, H.; Guan, Y.; Wang, P.; Gao, W.; Liu, L.; Cao, H.; Xiong, Z.; Vegge, T.; Chen, P. Ternary ruthenium complex hydrides for ammonia synthesis via the associative mechanism. *Nat. Catal.* **2021**, 4, 959-967.

19. Rösch, B.; Gentner, T. X.; Langer, J.; Färber, C.; Eyselein, J.; Zhao, L.; Ding, C.; Frenking, G.; Harder, S. Dinitrogen complexation and reduction at low-valent calcium. *Science* **2021,** *371* (6534), 1125.

20. Rosowski, F.; Hornung, A.; Hinrichsen, O.; Herein, D.; Muhler, M.; Ertl, G. Ruthenium catalysts for ammonia synthesis at high pressures: Preparation, characterization, and power-law kinetics. *Appl. Catal. A: Gen.* **1997,** *151* (2), 443-460.

21. Boudrifa, O.; Bouhemadou, A.; Uğur, Ş.; Khenata, R.; Bin-Omran, S.; Al-Douri, Y. Structural, electronic, optical and elastic properties of the complex K_2PtCl_6-structure hydrides

1 $ARuH_6$ (A = Mg, Ca, Sr and Ba): first-principles study. *Philosophical Magazine* **2016,** *96* (22),
2 2328-2361.

3 22. Logadóttir, Á.; Nørskov, J. K. Ammonia synthesis over a Ru(0001) surface studied by
4 density functional calculations. *J. Catal.* **2003**, 220 (2), 273-279.

5 23. Kozuch, S.; Shaik, S. How to Conceptualize Catalytic Cycles? The Energetic Span
6 Model. *Acc. Chem. Res.* **2011,** *44* (2), 101-110.

7

8

1 For Table of Contents only:

2 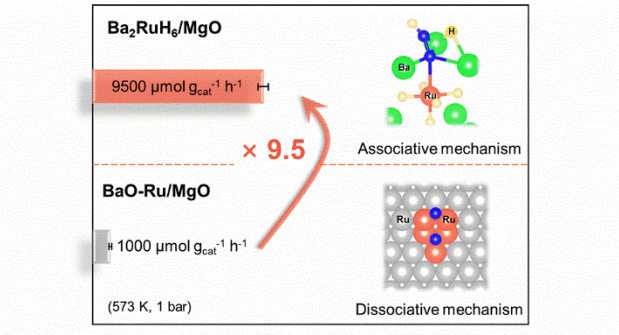

3